Semiconductor Physics, Quantum Electronics & Optoelectronics, 2008. V. 11, N 4. P. 370-380.

PACS 68.03.Cd, 68.35.Gy, 77.80.-e, 77.84.Dy

Polar properties and local piezoelectric response of ferroelectric nanotubes

A.N. Morozovska[1]*, G.S. Svechnikov[1], E.I. Shishkin[2], V.Y. Shur[2]
[1]*V. Lashkaryov Institute of Semiconductor Physics, National Academy of Science of Ukraine*
41, prospect Nauky, 03028 Kyiv, Ukraine
[2]*Institute of Physics and Applied Mathematics, Ural State University, 620083 Ekaterinburg, Russia*
**Corresponding author e-mail: morozo@i.com.ua*

Abstract. We consider the polar properties of the ferroelectric nanotubes within the framework of Landau-Ginzburg-Devonshire phenomenology. The approximate analytical expression for the paraelectric-ferroelectric transition temperature dependence on the radii of nanotube, polarization gradient, extrapolation length, elastic stresses and strains arising from surface tension and thermal expansion mismatch, and electrostriction coefficient was derived. We calculated *effective local piezoresponse* of the ferroelectric nanotube within decoupling approximation of electric and elastic problem. Obtained results explain the ferroelectricity conservation in $Pb(Zr,Ti)O_3$ and $BaTiO_3$ nanotubes observed by using Piezoelectric Force Microscopy.

Keywords: polar properties, ferroelectric nanotube, effective local piezoresponse, piezoelectric force microscopy.

Manuscript received 18.09.08; accepted for publication 20.10.08; published online 11.11.08.

1. Introduction

Ferroelectric nanotubes and nanorods are actively studied in nano-physics and nano-technology [1-5]. In many cases they demonstrate such polar properties as remnant polarization [1] and local piezoelectric hysteresis [3-5].

It is generally accepted, that the ferroelectric properties disappear under the particle size decreases below the critical one [6]. Actually, it is well known that depolarization electric field exists in the majority of confined ferroelectric systems [7] and causes the size-induced ferroelectricity disappearance in thin films and spherical particles [8].

However, the cylindrical geometry does not destroy ferroelectric phase (in contrast to size-induced paraelectric phase in spherical particles [9-15]), but sometimes the noticeable enhancement of ferroelectric properties appears [1-5, 16]. For instance, Yadlovker and Berger [1] reported about the spontaneous polarization enhancement up to 0.25-2 $\mu C/cm^2$ and ferroelectric phase conservation in Rochelle salt nanorods. With the help of Piezoelectric Force Microscopy (PFM), Morrison *et al.* [4, 5] demonstrated that $PbZr_{0.52}Ti_{0.48}O_3$ (PZT) nanotubes (radius R = 500-700 nm, thickness h = 50-70 nm, length 50 μm) possesses rectangular shape of the local piezoelectric response hysteresis loop with effective remnant piezoelectric coefficient value compatible with the ones typical for PZT films. Also, the authors demonstrated that the ferroelectric properties of the free $BaTiO_3$ nanotubes are perfect. Poyato *et al.* [17] with the help of PFM found that nanotube-patterned ("honeycomb") $BaTiO_3$ film of thickness 200-300 nm reveal ferroelectric properties. The inner diameter of the nanotubes ranged from 50 to 100 nm. Also, they demonstrated the existence of local piezoelectric and oriented ferroelectric responses, prior to the application of a dc field, in nanotubes-patterned $BaTiO_3$ thin films on Ti substrates synthesized hydrothermally at 200 °C. The phenomenological description of ferroelectricity enhancement in cylindrical nanoparticles has been recently proposed [18-20].

In our consideration of ferroelectric nanotube, we suppose that a nanoparticle surface is covered with a charged layer consisted of the free carriers adsorbed from the ambient (e.g., air with definite humidity or pores filled with a precursor solution). For instance, a thin water layer condensates on the polar oxide surface in the air with humidity 20-50 % [21]. The surface charges screen the surrounding template (usually Si or alumina porous matrix [1, 16] or regular 2D photonic crystal [3-5]) from the nanoparticle electric field, but the depolarization field inside the particle is caused by inhomogeneous polarization distribution. Thus, one could calculate the depolarization field inside a cylindrical nanoparticle under the short-circuit conditions proposed by Kretschmer and Binder [22].

For the case when a liquid precursor of ferroelectric (e.g. RS, PZT, SBT or BTO) filled the porous template by capillary effects [1], the uniform stress inside the pores is caused by surface tension [18]. During the following annealing both the thermal stresses and misfit strain on the tube-pore interface usually appear. In most of cases the stress causes the thin strained layer ("shell") on the tube-pore interface. For instance, Luo *et al.* [3] and Morrison *et al.* [4, 5] reported about amorphous PZT layer of thickness $\Delta h \approx$ 5-20 nm that clamped the nanotube crystalline "core". The shell may be partially removed by selective etching.

Using the experimental background, we modified the core-and-shell model of spherical ferroelectric nanoparticles proposed earlier by Niepce *et al.* [23, 24] and Glinchuk *et al.* [25] for the description of ferroelectric nanotubes polar properties. Firstly, we obtained the solution of elastic problem for the stress distribution inside the tube covered with thin strained shell. Then the polarization distribution inside the core was obtained and approximate analytical expression for paraelectric-ferroelectric transition temperature dependence on the nanotube thickness and radius, effective stress, polarization gradient and electrostriction coupling coefficients was derived. Note that the stress is caused by the particle surface clamping by template, i.e. it is related to surface tension, thermal expansion and mismatch strain [26]. We proved that the reason of the polar properties enhancement and conservation in ferroelectric nanotubes is the stress coupled with polarization via electrostriction effect under the strong decrease of depolarization field with tube length increase. Within decoupling approximation of electric and elastic problem [27, 28], we calculated the tube PFM response and compared calculations with available experimental data.

2. Free energy of a nanotube in the core and shell model

Let us consider the ferroelectric cylindrical nanotube of outer radius R_o, inner radius R_i, thickness $h = R_o - R_i$ and height l (see Fig. 1). The tube "core" of thickness $h - \Delta h$ is covered with thin amorphous "shell" of thickness $\Delta h << h$. The core polarization P_3 is oriented along z-axes. The external electric field is $\mathbf{E} = (0,0,E_0)$.

For the case when a liquid precursor of ferroelectric filled the porous template by capillary effects, the uniform stress $\sigma_{ij} = -p_o\delta_{ij}$ is caused by surface tension $p_o = 2\mu/R_o$ [18], where the coefficient μ could be related to the effective surface tension. During the following thermal annealing the cubic structured or even amorphous shell layer of thickness $\Delta h << R_o$ appears at the nanotube-template interface. The nanotube crystalline core is strained allowing for the thermal expansion and growth deformations as well as the surface tension frozen up inside the shell. Even after the

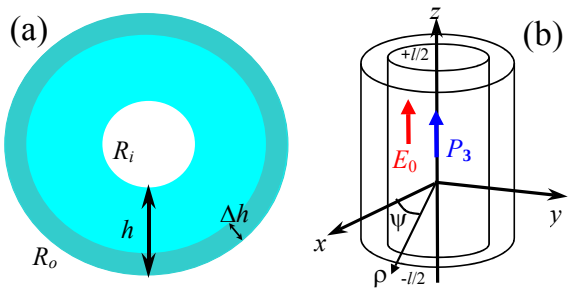

Fig. 1. (a) Cross-section of the ferroelectric nanotube with "shell" of thickness Δh and "core" of thickness $h - \Delta h$. (b) Geometry of calculations in cylindrical coordinates $\{\rho, \psi, z\}$.

template removal, the internal strain $u_{ij} = u_t\delta_{ij}$ is different inside core and shell. Namely, the shell strain u_t^s is determined by the effective surface tension p_o, growth deformation u_g and thermal expansion during annealing at temperature T_a, i.e. $u_t^s = -p_o(s_{11} + 2s_{12}) + \vartheta_i^s\Delta T + u_g$, whereas the core strain is determined by the thermal expansion only, i.e. $u_t^c = \vartheta_i^c\Delta T$ (here s_{11} and s_{12} are the elastic compliances, ϑ_i^c and ϑ_i^s are the linear temperature expansion coefficients of the tube core and shell, $\Delta T = T - T_a$ is the temperature change, see e.g. [29, 30]). The difference $\Delta u = u_t^c - u_t^s$ determines the core stress σ_{ij}^c as:

$$\sigma_{11}^c + \sigma_{22}^c \approx \sigma_{33}^c \approx \sigma(R_o, R_i),$$
$$\sigma(R_o, R_i) = -\frac{\Delta u}{s_{11} + s_{12}}\frac{2R_o\Delta h}{(R_o + R_i)h}, \qquad (1)$$
$$\Delta u = \frac{2\mu}{R_o}(s_{11} + 2s_{12}) + (\vartheta_i^c - \vartheta_i^s)\Delta T - u_g.$$

The Euler-Lagrange equation for the polarization can be obtained by the variation on polarization of the free energy functional $G = G_V + G_S$, consisting of the bulk part G_V and the surface one G_S. The bulk part G_V acquires the form:

$$G_V = \int_{-l/2}^{l/2} dz \int_0^{2\pi} d\psi \int_{R_i}^{R_o - \Delta h} \rho d\rho \times \left(\frac{\alpha_R(T)}{2} P_3^2 + \right.$$
$$\left. + \frac{\beta_R}{4} P_3^4 + \frac{\gamma}{6} P_3^6 + \frac{\delta}{2}(\nabla P_3)^2 - P_3\left(E_0 + \frac{E_3^d}{2} \right) \right). \qquad (2)$$

Material coefficients $\delta > 0$ and $\gamma > 0$, coefficient $\beta < 0$ for the first order phase transitions or $\beta > 0$ for the second order ones. The depolarization field is denoted by E_3^d. The coefficients $\alpha_T(T)$ and β_R is renormalized by elastic stresses σ_{ii}^c as

$$\alpha_R(T,R_o,R_i)=\alpha_T\left(T-T_C\right)+2\left(Q_{12}+Q_{11}\right)\times \times\frac{\Delta u}{s_{11}+s_{12}}\frac{2R_o\Delta h}{\left(R_o+R_i\right)h}, \tag{3}$$

$$\beta_R(R_o,R_i)= =\beta+2\frac{\left(Q_{11}^2+Q_{12}^2\right)s_{11}-2Q_{11}Q_{12}s_{12}}{s_{11}^2-s_{12}^2}\frac{2R_o\Delta h}{\left(R_o+R_i\right)h}. \tag{4}$$

Here, parameters T_C and Q_{ij} are respectively the Curie temperature and electrostriction coefficient of the bulk material; α_T is proportional to the inverse Curie constant.

Note that under the condition $R_{o,i}\to\infty$ the renormalization given by Eqs. (3)-(4) coincides with the ones obtained for thin strained films by Pertsev *et al.* [30] allowing for stress relaxation [31], namely $\sigma(h)\approx\frac{\Delta u}{s_{11}+s_{12}}\frac{\Delta h}{h}$, here Δh could be related with characteristic distance h_d of stress relaxation and $\Delta u\to u_m$. In other words, we obtained that the stress relaxation occurs inside the shell. When $\Delta h\to 0$ the nanotube crystalline core appeared almost unstrained, i.e. $\sigma\approx 0$.

The surface part of the polarization-dependent free energy G_S is thought to be proportional to square of polarization on the particle surface S, namely $G_S=\frac{\delta}{2}\int_S\frac{ds}{\lambda}P_S^2$ (λ is the extrapolation length [8, 9]). The considered nanotube has upper and bottom surfaces $z=l/2$, $z=-l/2$ and sidewalls $\rho=R_i$, $\rho=R_o-\Delta h$, so its surface energy G_S acquires the form:

$$G_S=\delta\int_0^{2\pi}d\psi\left(\int_{-l/2}^{l/2}dz\left(\frac{R_o}{\lambda_S}P_3^2(\rho=R_o-\Delta h)+\frac{R_i}{\lambda_S}P_3^2(\rho=R_i)\right)+ +\int_{R_i}^{R_o-\Delta h}\frac{\rho}{\lambda_b}d\rho\left(P_3^2\left(z=\frac{l}{2}\right)+P_3^2\left(z=-\frac{l}{2}\right)\right)\right). \tag{5}$$

We introduced longitudinal and lateral extrapolation lengths $\lambda_b\neq\lambda_S$. Hereinafter, we regard these extrapolation lengths positive.

Variation of the free energy expression $\delta G/\delta P_3=0$ yields the Euler-Lagrange equations with the boundary conditions on the tube faces $z=\pm l/2$ and the sidewalls $\rho\approx R_{o,i}$. Under the presence of *lattice pinning of viscous friction type*, the polarization distribution should be found from Landau-Khalatnikov equation $\delta G/\delta P_3=-\Gamma\,\partial P_3/\partial t$, where Γ in kinetic coefficient. Along with the Poisson equation for the depolarization field $E_3^d=-\partial\varphi/\partial z$ they form the closed system:

$$\begin{cases}\Gamma\dfrac{\partial}{\partial t}P_3+\alpha_R P_3+\beta_R P_3^3+\gamma P_3^5- -\delta\left(\dfrac{\partial^2}{\partial z^2}+\dfrac{1}{\rho}\dfrac{\partial}{\partial\rho}\rho\dfrac{\partial}{\partial\rho}+\dfrac{1}{\rho^2}\dfrac{\partial^2}{\partial\psi^2}\right)P_3=E_0+E_3^d,\\ \left(P_3+\lambda_b\dfrac{dP_3}{dz}\right)\Big|_{z=l/2}=0,\\ \left(P_3-\lambda_b\dfrac{dP_3}{dz}\right)\Big|_{z=-l/2}=0,\\ \left(P_3+\lambda_S\dfrac{dP_3}{d\rho}\right)\Big|_{\rho=R_o}=0,\\ \left(P_3-\lambda_S\dfrac{dP_3}{d\rho}\right)\Big|_{\rho=R_i}=0,\end{cases} \tag{6}$$

$$\begin{cases}\left(\dfrac{\partial^2}{\partial z^2}+\dfrac{1}{\rho}\dfrac{\partial}{\partial\rho}\rho\dfrac{\partial}{\partial\rho}+\dfrac{1}{\rho^2}\dfrac{\partial^2}{\partial\psi^2}\right)\varphi=4\pi\,\mathrm{div}\,\mathbf{P},\\ \varphi(\rho=R_{o,e})=0,\quad \varphi\left(z=\pm\dfrac{l}{2}\right)=0.\end{cases} \tag{7}$$

The polarization distribution in the ferroelectric phase should be found by direct variational methods allowing for possible polydomain states appearance in confined particles. At $(\lambda_S/R_o)<<1$ an exact series for the polarization and depolarization field distributions can be obtained [18]. The inequality $(\lambda_S/R_o)<<1$ is valid for typical extrapolation lengths $\lambda_S=0.3$-5 nm and radii $R_o=30$-500 nm. Substituting the series for depolarization field and polarization into the free energy G and integrating over nanoparticle volume, we obtained the free energy with renormalized coefficients for the average polarization. For infinite tubes and wires, the single-domain state is energetically preferable, since the depolarization field is absent and correlation energy is minimal for single-domain case. The depolarization field is highest for a single-domain nanotube, namely its upper estimation has the form:

$$E_3^d(\rho,z)=-\frac{4\pi}{1+\left(k_{01}l/2\pi R_o\right)^2}\times \times\left(P_3(\rho,z)-\frac{2}{l}\int_{-l/2}^{l/2}dzP_3(\rho,z)\right). \tag{8}$$

Hereinafter, $k_{01}(R_o,R_i)$ is the lowest root of the equation $J_0\left(k_{01}\frac{R_i}{R_o}\right)N_0(k_{01})-J_0(k_{01})N_0\left(k_{01}\frac{R_i}{R_o}\right)=0$ ($J_0(x)$ and $N_0(x)$ are Bessel and Neiman functions of zero order, respectively). It should be noted that the depolarization field is absent outside the particles in the framework of our model. Therefore, the interaction of such nanoparticles is practically absent due to the screening. Their composite can be considered as the assembly of independent particles.

For finite polydomain tubes, only numerical simulations have been performed. However, simple approximate analytical expression for the free energy renormalized coefficients has been obtained for the infinite single-domain tubes. We report the results below.

3. Phase diagram of the long nanotubes

We derived the interpolation for the paraelectric-ferroelectric transition temperature $T_{CR}(R_o, R_i)$ of the long nanotubes (for $l >> R_o$ depolarization field $E_d \to 0$ in accordance with Eq. (8)):

$$T_{CR}(R_o, R_i) = T_C + \frac{2(Q_{11}+Q_{12})}{\alpha_T}\sigma(R_o, R_i) - \\ -\delta\frac{k_{01}^2(R_o, R_i)}{\alpha_T R_o^2}. \qquad (9)$$

An expression for the stress $\sigma(R_o, R_i)$ is given by Eqs (1). The first term in Eq. (9) is the bulk transition temperature, the second term is related to the coupling of stress with polarization via electrostriction effect, the third term is caused by correlation effects. The correlation term is always negative and thus only decreases the transition temperature, whereas the electrostriction term in Eq. (9) could be positive or negative depending on the sign of $(Q_{11} + Q_{12})\sigma$. Note that both signs of $(Q_{11} + Q_{12})$ are possible for different ferroelectrics, however $(Q_{11} + Q_{12}) > 0$ for most of the perovskite ferroelectrics. Below, we demonstrate that increasing of transition temperature and thus ferroelectric properties conservation or even enhancement is possible, when the stress is compressive ($\sigma < 0$) and depolarization field is small enough.

Taking into account that the correlation radius at zero temperature is several (up to ten) lattice constants $\sqrt{\delta/\alpha_T T_C} \sim 1-4\,\text{nm}$ (see, e.g., experimental data of Rodriguez *et al.* [32]) and using expression (1) for the stress, we introduced the parameters and dimensionless variables that correspond to the lattice constant units:

$$R_m = \frac{2(Q_{11}+Q_{12})}{\alpha_T T_C}\frac{(\vartheta_i^e - \vartheta_i^s)\Delta T - u_g}{s_{11}+s_{12}},$$

$$R_\mu = \frac{4(Q_{11}+Q_{12})}{\alpha_T T_C}\frac{\mu}{R_S}\frac{s_{11}+2s_{12}}{s_{11}+s_{12}}, \qquad (10a)$$

$$R_S = \sqrt{\frac{\delta}{\alpha_T T_C}}, \qquad r_o = \frac{R_o}{R_S}, \qquad r_i = \frac{R_i}{R_S},$$

$$w = \frac{h}{R_S}, \qquad \Delta w = \frac{\Delta h}{R_S}. \qquad (10b)$$

Using approximate formula $k_{01}(x) \approx \pi/(1-x) - (1-x)/\left(4(1-x)^2 + 8\pi x\right)$ for $x \to 1$, where $x = r_i / r_o$ one can write in dimensionless variables:

$$T_{CR}(w, r_i, r_o) \approx T_C\left(1 - \left(\frac{R_\mu}{r_o} + R_m\right)\times\right. \\ \left.\times\frac{2r_o}{r_o + r_i}\frac{\Delta w}{w} - \left(\frac{\pi^2}{w^2} - \frac{\pi/2}{w^2 + 2\pi r_o r_i}\right)\right), \qquad (11)$$

Let us make some estimations of the second and third terms in Eq. (11) for perovskites $BaTiO_3$ and $Pb(Zr,Ti)O_3$. Using parameters $Q_{11} = 0.11\ \text{m}^4/\text{C}^2$, $Q_{12} = -0.043\ \text{m}^4/\text{C}^2$, $T_C = 400$ K, $\alpha_T = -7.4\cdot10^{-5}\ \text{K}^{-1}$ ($BaTiO_3$) and $Q_{11} = 0.089\ \text{m}^4/\text{C}^2$, $Q_{12} = -0.046\ \text{m}^4/\text{C}^2$, $T_C = 666$ K, $\alpha_T = -3\cdot10^{-5}\ \text{K}^{-1}$ ($PbZr_{0.5}Ti_{0.5}O_3$); $s_{11} = 8\cdot10^{-12}$ Pa, $s_{12} = -2.5\cdot10^{-12}$ Pa, $\Delta u \sim 5\cdot(10^{-3}\text{-}10^{-2})$ for por-Si or Al_2O_3 templates, $\mu = 0.5\text{-}5$ N/m (see, e.g., Ref. [13]), we obtained that $R_\mu \sim 0.06\text{-}0.6$, $|R_m| \approx 0.5\text{-}5$ and $\Delta w \sim 0.2\text{-}2$, respectively. Hence, both terms are comparable with unity and their contributions should be calculated carefully for the material under consideration.

The dependences of transition temperature $T_{CR}(w, r_i, r_o)$ on tube thickness w for the cases of compressed ($R_m < 0$, solid curves), unstrained ($\Delta w = 0$, dashed curves) and tensiled ($R_m > 0$, dotted curves) tubes are compared in Fig. 2a. Corresponding spontaneous polarization $P_3(T) = \sqrt{-\alpha_R(T)/\beta_R}$ temperature dependences are presented in Fig. 2b. It is clear that nanotube compression leads to the maximum $T_{\max} > T_C$ on transition temperature thickness dependence and to the corresponding enhancement of spontaneous polarization $P_3(T) > P_S(T)$ in the temperature range $T \approx T_{\max}$, whereas unstrained and tensiled nanotubes reveal monotonic dependences $T_{CR}(w, r_i, r_o) < T_C$ with deteriorated polar properties $P_3(T) < P_S(T)$. Let us underline that the height and sharpness temperature maximum observed for compressed tubes decreases under the decrease of shell layer thicknesses Δw.

For the important case of thin tubes ($w << r_i$) one obtains from Eq. (11):

$$T_{CR}(w) \approx T_C\left(1 - R_m\frac{\Delta w}{w} - \frac{\pi^2}{w^2}\right). \qquad (12)$$

Under the condition $R_m < 0$, the second term tends to increase T_{CR}, while the third one always decreases it. At $R_m < 0$, the competition between the contribution of strain effect represented by the second term and the correlation effect represented by the third one leads to the maximum appearance in $T_{CR}(w)$ dependence, namely:

$$T_{\max}(w_{\max}) \approx T_C\left(1 + \frac{R_m^2 \Delta w^2}{4\pi^2}\right), w_{\max} \approx -\frac{2\pi^2}{R_m \Delta w}. \qquad (13)$$

For thin tubes, we also obtained simple analytical expressions for the critical radius at given temperature T:

$$w_{cr}^{\pm}(T) \approx \frac{R_m\Delta w \pm \sqrt{4\pi^2(1 - T/T_C) + R_m^2\Delta w^2}}{2(1 - T/T_C)}. \qquad (14)$$

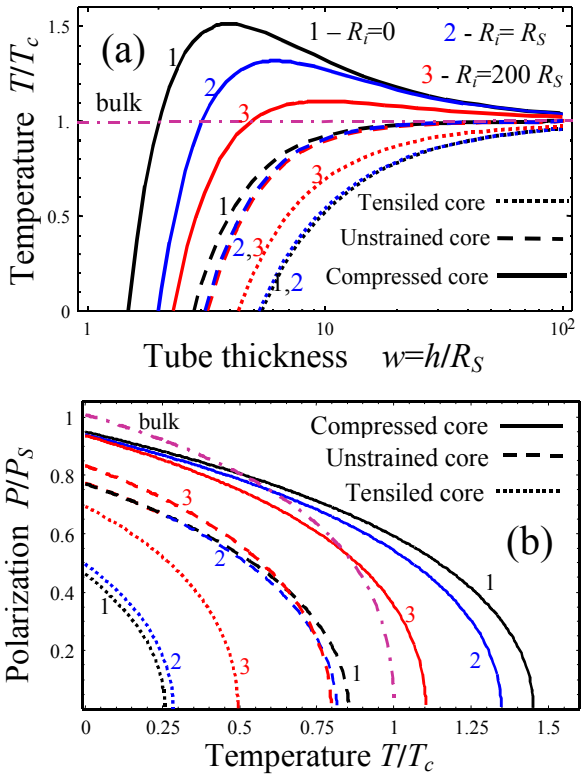

Fig. 2. (a) Transition temperature via tube thickness w and (b) spontaneous polarization temperature dependence for tube thickness $w = 7$ calculated from Eq. (11) for $R_S = 4$ nm, $\Delta w = 0.5$, $R_\mu = 0.5$ (which corresponds to PZT 50/50 parameters), $r_i = 0$; 1; 200 (curves 1, 2, 3), $R_m = -4$ (solid curves), $R_m = 0$ (dashed curves), $R_m = +4$ (dotted curves). Dashed-dotted curves correspond to the bulk material with spontaneous polarization $P_S(T)$.

Sign "+" before the radical in Eq. (14) corresponds to the both cases of unstrained, tensiled or compressed tubes (i.e., both signs of R_m), while both signs "±" have sense for compressed tubes (i.e. two roots may exist at $R_m < 0$) under the condition $T > T_C$.

Finally let us discuss the influence of quartic term renormalization β_R given by Eq. (4) on nanotubes phase diagrams in the particular case of the first order phase transitions in bulk material, i.e. when $\beta < 0$. Since $\beta_R = \beta + \Delta\beta \dfrac{2r_o \Delta w}{(r_o + r_i)w}$ in accordance with Eq. (4), the situation $\beta_R > 0$ could appear at some tube thicknesses when $\Delta\beta > 0$, i.e., the transition order in nanotube would be changed. This situation for $PbTiO_3$ nanotubes phase diagrams in coordinates tube thickness-inner radius is demonstrated in Fig. 3 at room temperature and different stress signs ($R_m < 0$, $R_m = 0$, $R_m > 0$).

For the chosen material parameters, compressed tubes phase diagrams (a) have the thinnest region of paraelectric phase (PE) and widest region of the second order ferroelectric phase (FE-II) in comparison with unstrained (b) and tensiled (c) tubes.

4. Piezoelectric force microscopy response of ferroelectric nanotubes

Recently Morrison *et al.* [4, 5] demonstrated that long $Pb(Zr,Ti)O_3$ and $BaTiO_3$ nanotubes possess perfect piezoelectric properties. For thin $PbZr_{52}Ti_{48}O_3$ nanotube (outer diameter 700 nm, wall thickness about 70 nm, length 30 μm) they obtained rectangular hysteresis loop of effective piezoelectric response $d_{33}^{\text{eff}}(U)$. Poyato *et al.* [17] with the help of PFM found that nanotube-patterned

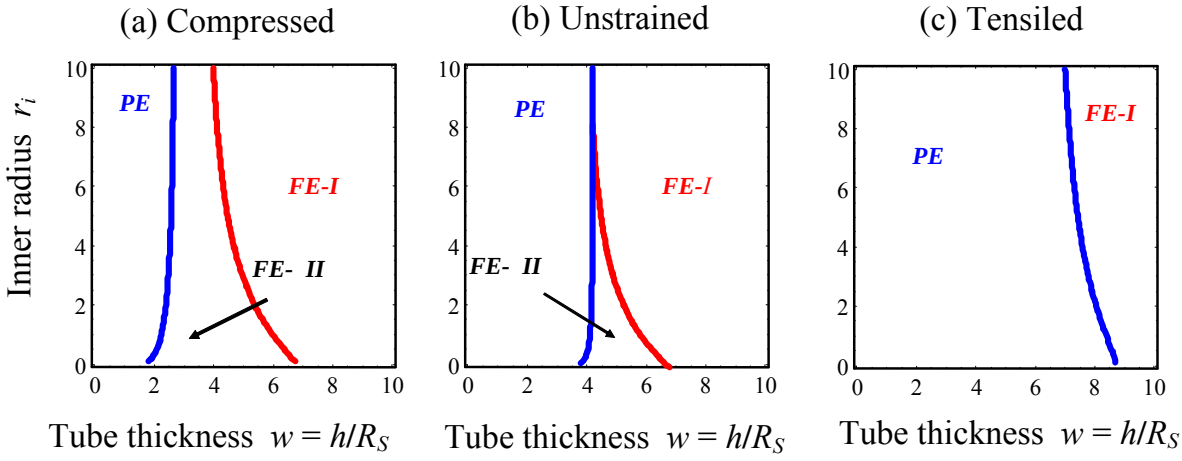

Fig. 3. Phase diagram in coordinates $\{r_i, w\}$ calculated at room temperature $T = 297$ K, $R_S = 4$ nm, $\Delta w = 0.5$, $R_\mu = 0.2$, $R_m = -4$ (a), $R_m = 0$ (b), $R_m = +4$ (c). Material parameters correspond to $PbTiO_3$; PE – paraelectric phase, FE – ferroelectric phases of the first (I) and second (II) orders.

$BaTiO_3$ films of thickness 200-300 nm reveal piezoelectric hysteresis.

The effective vertical piezoresponse d_{33}^{eff} is determined by the vertical mechanical displacement u_3 of ferroelectric sample surface caused by *inhomogeneous* electric field of a PFM probe biased under the voltage U, namely $d_{33}^{\text{eff}}(U) = u_3/U$ (see e.g. Refs. [33-35]). The local PFM response d_{33}^{eff} is proportional to the stress piezoelectric tensor coefficients $d_{klj}(\mathbf{r})$ representing ferroelectric material properties convoluted with the appropriate elastic Green function $G_{ij}(\mathbf{r},\xi)$ [33-35]. Extending the results of Refs. [35, 37] for an empty tube embedded into non-piezoelectric matrix, we obtained that

$$d_{33}^{\text{eff}}(U) = \int_{-\infty}^{\infty} d\xi_1 \int_{-\infty}^{\infty} d\xi_2 \int_{0}^{\infty} d\xi_3 \frac{\partial G_{ij}(x-\xi_1, y-\xi_2, \xi_3)}{\partial \xi_k} \times$$
$$\times E_l(\xi) \cdot c_{kjmn} d_{lnm}(y_1+\xi_1, y_2+\xi_2, \xi_3)$$
$$\approx t_{13}(R_o, R_i, a, \vartheta, \nu) d_{31}(U) + t_{51}(R_o, R_i, a, \vartheta) \times$$
$$\times d_{15}(U) + t_{33}(R_o, R_i, a, \vartheta) d_{33}(U). \qquad (15)$$

The inhomogeneous electric field $E_k(\mathbf{r}) = -\partial\varphi/\partial x_k$ is produced by the PFM tip inside of the sample, c_{kjmn} are stiffness tensor components. Rather cumbersome integrals $t_{13}(R_o, R_i, a, \gamma, \nu)$ depend only on tube outer and inner radiuses, dielectric anisotropy coefficient $\vartheta = \sqrt{\varepsilon_{33}/\varepsilon_{11}}$, Poisson ratio ν and probe electric field distribution and tip position a with respect to the tube (see Fig. 4a). In the approximation of effective point charge Q simulating the probe electric field, the distance between the sample surface and the effective point charge is $d_Q = \varepsilon_e r_0 / \sqrt{\varepsilon_{11}\varepsilon_{33}}$ (r_0 is the probe apex curvature, ε_e is ambient permittivity, $d_Q \sim 10$ nm). In accordance with Eq. (15), the effective piezoresponse d_{33}^{eff} polarization dependence is fully determined by piezoelectric coefficients averaged over the piezoresponse volume. The conventional relationships between piezoelectric coefficients $d_{ijk} = 2\varepsilon_0 Q_{jklm} \langle \varepsilon_{il} P_m \rangle$ in Voigth notation acquire explicit form:

$$d_{33} = 2\varepsilon_0 Q_{11} \langle \varepsilon_{33} P_3 \rangle, \quad d_{31} = 2\varepsilon_0 Q_{12} \langle \varepsilon_{33} P_3 \rangle,$$
$$d_{15} = 2\varepsilon_0 Q_{44} \langle \varepsilon_{11} P_3 \rangle. \qquad (16)$$

Q_{ij} is electrostriction tensor components in the Voigth notation.

In Table 1, we summarized calculated values of thermodynamic coercive field $E_c = 2\sqrt{-\alpha_R^{\,3}/27\beta_R}$, spontaneous polarization P_S, dielectric permittivity ε_{33} at room temperature, critical thickness h_{cr} and Curie temperature T_C for compressed ($\Delta u < 0$), unstrained ($\Delta u = 0$) and tensiled ($\Delta u > 0$) PZT (50/50) nanotubes (first 3 rows) in comparison with bulk material (last row). In the last columns of the table, we presented the values of electric field $E_Q(\rho, z) \cong U \dfrac{\left(\sqrt{\varepsilon_{11}/\varepsilon_{33}}\, z + d_Q\right)\sqrt{\varepsilon_{11}/\varepsilon_{33}}\, d_Q}{\left(\rho^2 + \left(\sqrt{\varepsilon_{11}/\varepsilon_{33}}\, z + d_Q\right)^2\right)^{3/2}}$ produced by the PFM tip with parameter $d_Q \approx$ 25-50 nm on the tube surface $z = 0$ and in the depth $z = d_Q$ for the coercive voltage $U_c^{\pm} \approx 2.5\text{V}$ measured experimentally. Material parameters used in calculations are given in Table 2 of Appendix A.

It is clear that obtained values of $E_Q(0,0)$ is in order of magnitude higher than thermodynamic coercive field E_c. The result is expectable, since in order to reverse the polarization inside the domain the PFM tip field should be higher than the coercive one not only just below the tip ($z = 0$, $\rho = 0$) but also inside the layer of depth about d_Q (typical penetration depth of piezoresponse) [36, 37]. The values $E_Q(0, z = d_Q)$ actually appeared ten times smaller than $E_Q(0,0)$ and in a good agreement with calculated E_c values.

We compare the piezoresponse loop shape obtained for $PbZr_{52}Ti_{48}O_3$ nanotube [4] and $BaTiO_3$ honeycomb [17] with our theoretical calculations in Figs. 4.

Table 1.

Tubes PZT (50/50)	Strain Δu (%)	E_c (kV/cm)	P_S (μC/cm^2)	ε_{33}	h_{cr} (nm)	T_C (K)	$E_Q(0, 0)$ (kV/cm)	$E_Q(0, d_Q)$ (kV/cm)
Sizes:	–1	209	45	398	12.3	704	2060-1030	219-110
R_o=700 nm,	0	167	42	474	16.8	645	1900-950	227-113
h = 70 nm,	1	128	39	583	23.0	586	1700-850	232-116
Δh = 7 nm								
Bulk PZT (50/50)		228	50	375	—	666	2100-1050	214-107

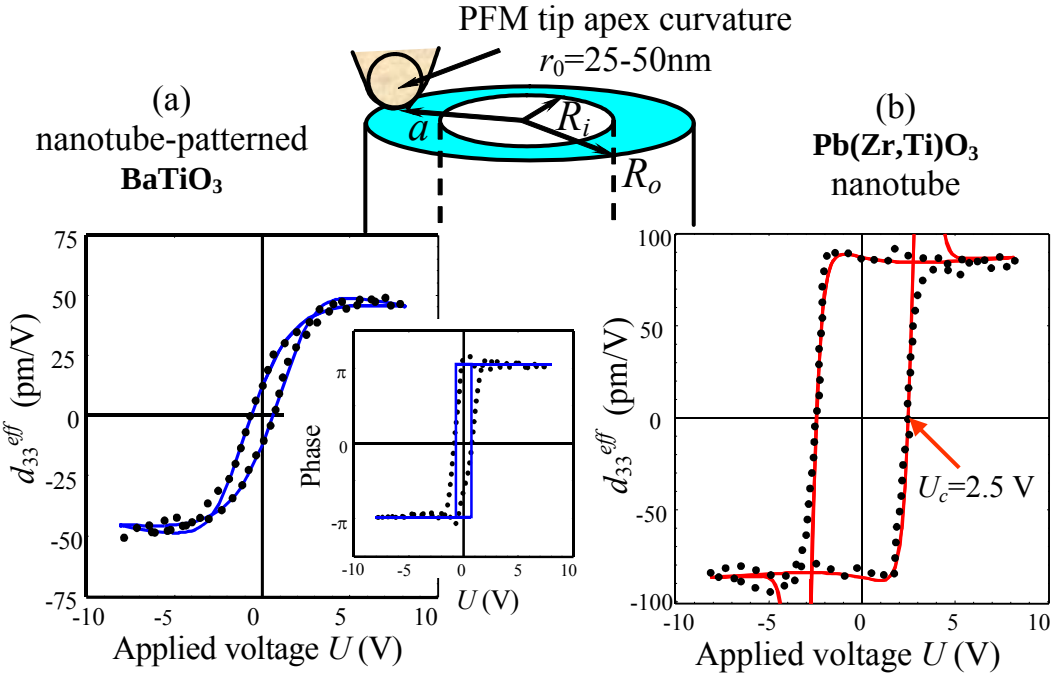

Fig. 4. (a) Effective piezoresponse d_{33}^{eff} of $PbZr_{52}Ti_{48}O_3$ nanotube (outer diameter 700 nm, wall thickness 90 nm, length about 30 μm) vs. applied voltage U. Squares are experimental data of Morrison *et al.* [4], solid curve is our fitting (13) for $R_S \approx 7$, $\Delta r = 5$, $R_\mu = -5$, $\vartheta = 0.25$ and PZT material parameters. (b) Effective piezoresponse d_{33}^{eff} of nanotube-patterned $BaTiO_3$ "honeycomb" (inner radius 50-100 nm, film thickness about 200-300 nm) vs. applied voltage U. Squares are experimental data of Poyato *et al.* [17], solid curve is our fitting at $R_i = 50$ nm, $R_o = 62$ nm, $R_S \approx 6$, $\Delta r = 5$, $R_\mu = -5$ and $BaTiO_3$ material parameters. Dimensionless frequency of external field $\omega\Gamma/(\alpha_T T_C) = 0.15$, $\sqrt{\delta} = 1\,\text{nm}$.

5. Conclusions

- We reported ferroelectricity conservation and enhancement in long perovskite nanotubes compressed by their shell in contrast to ferroelectricity degradation in perovskite nanotubes tensiled by their shell. We demonstrated the stress-induced change of the ferroelectric phase transition order.
- The anisotropic stress as well as depolarization field decrease in long nanotubes are the keys to the ferroelectricity conservation. While the influence of depolarization field is obvious, the role of radial stress can be qualitatively understood as follows: although the radial stress conserves the inversion center, it leads to the short-range forces strengthening in lateral direction (caused by the bond contraction) and their weakening in z-direction (caused by the bond elongation). As a result, the long-range correlations become more pronounced in polar direction in comparison with the short-range forces.
- We calculated the tube PFM response and demonstrated reasonable agreement with available experimental data.

Acknowledgements

Authors gratefully acknowledge the financial support from National Academy of Science of Ukraine, grant, joint Russian-Ukrainian grant NASU N 17-Ukr_a (RFBR N 08-02-90434), Ministry of Science and Education of Ukraine.

Appendix A. Free energy with coefficients renormalized by elastic stresses

Let us consider the nanotube with sidewalls covered with thin surface layers (shell). The free energy expansion on polarization $\mathbf{P} = (0, 0, P_3)$ and stress σ_{ij} powers has the form:

$$G_V = \int_{-l/2}^{l/2} dz \int_0^{2\pi} d\psi \int_{R_i}^{R_o} \rho d\rho \left(\begin{array}{l} a_1 P_3^2 + a_{11} P_3^4 + a_{111} P_3^6 - Q_{11}\sigma_{33} P_3^2 - Q_{12}(\sigma_{11} + \sigma_{22}) P_3^2 - \\ -(\sigma_{11} + \sigma_{22} + \sigma_{33})\, u_t - \frac{1}{2} s_{11}\left(\sigma_{11}^2 + \sigma_{22}^2 + \sigma_{33}^2\right) - \\ - s_{12}(\sigma_{11}\sigma_{22} + \sigma_{11}\sigma_{33} + \sigma_{33}\sigma_{22}) - \frac{1}{2} s_{44}\left(\sigma_{23}^2 + \sigma_{13}^2 + \sigma_{12}^2\right) \end{array} \right) \qquad \text{(A.1)}$$

Subscripts 1, 2 and 3 denote Cartesian coordinates *x*, *y* and *z*, respectively. Hereinafter, we use Voigt notation or matrix notation when it is necessary (*xx* = 1, *yy* = 2, *zz* = 3, *zy* = 4, *zx* = 5, *xy* = 6).

The internal isotropic strain $u_{ij} = u_t \delta_{ij}$, where $u_t = u_t^c \theta(R_m - \rho) + u_t^s \theta(\rho - R_m)$ is different in core and shell. Namely, $u_t^s = -2\mu\left(s_{11}^s + 2s_{12}^s\right)/R_o + \vartheta_i^s \Delta T + u_g$ at $\rho \in (R_i, R_m)$ and $u_t^c = \vartheta_i^c \Delta T$ at $\rho \in (R_m, R_o)$. Here the interface radius $R_m = R_o - \Delta h$ is introduced. The temperature change after annealing is $\Delta T = T - T_a$, and $\vartheta_i^{s,c}$ are the linear temperature expansion coefficients. Polarization P_3 exists in the core region ("c") only, i.e. $P_3(\rho) = P_3(\rho)\theta(R_m - \rho)$. Hereinafter, superscripts "s" and "c" are related to the shell and core material, respectively. We will use them when necessary.

Minimization of the free energy (A.1) on stress components leads to the following equations of state:

$$\begin{cases} u_{11} = s_{11}\sigma_{11} + s_{12}(\sigma_{22} + \sigma_{33}) + Q_{12}P_3^2 + u_t, \\ u_{22} = s_{11}\sigma_{22} + s_{12}(\sigma_{11} + \sigma_{33}) + Q_{12}P_3^2 + u_t, \\ u_{33} = s_{11}\sigma_{33} + s_{12}(\sigma_{22} + \sigma_{11}) + Q_{11}P_3^2 + u_t, \\ 2u_{23} = s_{44}\sigma_{23}, \quad 2u_{13} = s_{44}\sigma_{13}, \quad 2u_{12} = s_{44}\sigma_{12}. \end{cases} \tag{A.2}$$

Here u_{ij} are the strain tensor components. Displacement vector components u_i determine the strain tensor as $u_{ij} = \left(\partial u_i / \partial x_j + \partial u_j / \partial x_i\right)/2$.

Distribution of mechanical displacement should satisfy the conditions of mechanical equilibrium $\partial\sigma_{ij}/\partial x_i = 0$ as well as the appropriate boundary conditions $n_i\sigma_{ij} = 0$ on the free surface and conditions of continuity at interfaces.

Let us introduce the cylindrical coordinates (ρ, ψ, *z*) with *z*-axis coinciding with tube symmetry axis. Due to the axial symmetry of the system, only ρ- and *z*-components of displacement are nonzero, u_ρ and u_z. In the general case, both of them may depend on ρ and *z*, e.g. for the homogeneous thermal expansion $u_\rho = \rho\,\vartheta\,\Delta T$, $u_z = z\,\vartheta\,\Delta T$. At the first approximation, we suppose that both displacement components depend only on one coordinate, namely $u_\rho(\rho)$ and $u_z(z)$. Then, we try to find a general solution from the conditions of mechanical equilibrium that satisfies all the boundary conditions.

For the given ansatz, the deformation tensor nontrivial components are $u_{zz} = \partial u_z/\partial z$, $u_{\rho\rho} = \partial u_\rho/\partial\rho$ and $u_{\psi\psi} = u_\rho/\rho$. Shear components of stress and strain are zero. In this case, equations $\partial\sigma_{ij}/\partial x_i = 0$ in the cylindrical coordinate system have the form:

$$\begin{cases} \dfrac{\partial\sigma_{zz}}{\partial z} = 0, \\ \dfrac{\partial\sigma_{\psi\psi}}{\partial\rho} + \dfrac{\sigma_{\rho\rho} - \sigma_{\psi\psi}}{\rho} = 0. \end{cases} \tag{A.3}$$

Thus, equations of state (S.2) can be rewritten as follows:

$$\begin{cases} \sigma_{\rho\rho} = c_{11}\upsilon_{\rho\rho} + c_{12}(\upsilon_{\psi\psi} + \upsilon_{zz}), \\ \sigma_{\psi\psi} = c_{11}\upsilon_{\psi\psi} + c_{12}(\upsilon_{\rho\rho} + \upsilon_{zz}), \\ \sigma_{zz} = c_{11}\upsilon_{zz} + c_{12}(\upsilon_{\psi\psi} + \upsilon_{\rho\rho}). \end{cases} \tag{A.4}$$

Where $\upsilon_{\rho\rho} = u_{\rho\rho} - u_t - Q_{12}P_3^2$, $\upsilon_{\psi\psi} = u_{\psi\psi} - u_t - Q_{12}P_3^2$, $\upsilon_{zz} = u_{zz} - u_t - Q_{11}P_3^2$ and elastic stiffness $c_{11} = (s_{11} + s_{12})/((s_{11} - s_{12})(s_{11} + 2s_{12}))$, $c_{12} = -s_{12}/((s_{11} - s_{12})(s_{11} + 2s_{12}))$ are introduced. After elementary transformations:

$$\begin{cases} u_z = a\,z, \quad u_\rho = b\,\rho + \dfrac{c}{\rho}, \\ u_{zz} = a, \quad u_{\rho\rho} = b - \dfrac{c}{\rho^2}, \quad u_{\psi\psi} = b + \dfrac{c}{\rho^2}. \end{cases} \tag{A.5a}$$

$$\begin{cases} \sigma_{\rho\rho} = a\,c_{12} + b(c_{11} + c_{12}) - \dfrac{c}{\rho^2}(c_{11} - c_{12}) - \\ - u_t(c_{11} + 2c_{12}) - (Q_{12}(c_{11} + c_{12}) + Q_{11}c_{12})P_3^2, \\ \sigma_{\psi\psi} = a\,c_{12} + b(c_{11} + c_{12}) + \dfrac{c}{\rho^2}(c_{11} - c_{12}) - \\ - u_t(c_{11} + 2c_{12}) - (Q_{12}(c_{11} + c_{12}) + Q_{11}c_{12})P_3^2, \\ \sigma_{zz} = a\,c_{11} + 2b\,c_{12} - u_t(c_{11} + 2c_{12}) - \\ - (Q_{11}\,c_{11} + 2Q_{12}c_{12})P_3^2. \end{cases} \tag{A.5b}$$

The boundary conditions of mechanical equilibrium $n_i\sigma_{ij} = 0$ on the external surfaces of a cylindrical solid body have the following form:

$$\begin{cases} \sigma_{\rho\rho}^s(\rho = R_o) = 0, \quad \sigma_{\rho\rho}^c(\rho = R_i) = 0, \\ \sigma_{zz}^c(z = \pm l/2, \rho \in (R_i, R_m)) = 0, \\ \sigma_{zz}^s(z = \pm l/2, \rho \in (R_m, R_o)) = 0. \end{cases} \tag{A.6}$$

On the interface between two different mediums ($\rho = R_m$), continuity conditions of stress tensor normal components and the displacement vector should be satisfied:

$$\begin{cases} \sigma_{\rho\rho}^s(\rho = R_m + 0) = \sigma_{\rho\rho}^c(\rho = R_m - 0), \\ u_\rho(\rho = R_m + 0) = u_\rho(\rho = R_m - 0), \\ u_z(\rho = R_m + 0) = u_z(\rho = R_m - 0). \end{cases} \tag{A.7}$$

Therefore, for the tube consisting of two layers, we have seven boundaries and interfacial conditions (A.4-8). At the same time, we have a general solution (A.3) for each layer, depending on the independent constants ($\{a^c, b^c, c^c\}$ and $\{a^s, b^s, c^s\}$) in each layer. For two layers, we have six constants, which do not allow us to fulfill seven independent conditions simultaneously. Since we are interested in the solution for a long tube, we have to satisfy the conditions on the lateral surfaces. As for the conditions on faces at $z = \pm l/2$, the natural way to solve this problem approximately is to nullify the overall force acting on the face of the tube, i.e. $\int_{R_o<\rho<R_i} \sigma_{zz}(z = \pm l/2, \rho)\rho d\rho = 0$ and obtain the solution in the sense of the Saint Venant principle.

Under the conditions $\Delta h << h$ and $P_3^2(l/2,\rho) = P_3^2(-l/2,\rho)$, we finally obtain the solution inside the core and shell regions:

$$\sigma_{11}^c + \sigma_{22}^c = \sigma_{\rho\rho}^c + \sigma_{\psi\psi}^c = -\frac{1}{s_{11}^s + s_{12}^s} \times \times \frac{2R_o\Delta h}{(R_o + R_i)h}\left[\Delta u + \frac{Q_{12}s_{11}^s - Q_{11}s_{12}^s}{s_{11}^s - s_{12}^s} P_3^2\right], \quad \text{(A.9a)}$$

$$\sigma_{33}^c = \sigma_{zz}^c = -\frac{1}{s_{11}^s + s_{12}^s} \times \times \frac{2R_o\Delta h}{(R_o + R_i)h}\left[\Delta u + \frac{Q_{11}s_{11}^s - Q_{12}s_{12}^s}{s_{11}^s - s_{12}^s} P_3^2\right], \quad \text{(A.9b)}$$

$$\sigma_{zz}^s = \frac{1}{s_{11}^s + s_{12}^s}\left[\Delta u + \frac{Q_{11}s_{11}^s - Q_{12}s_{12}^s}{s_{11}^s - s_{12}^s} \times \times \int_{R_m<\rho<R_i} \frac{2\rho\, d\rho}{R_m^2 - R_i^2} P_3^2(l/2,\rho)\right], \quad \text{(A.9c)}$$

$$\sigma_{\rho\rho}^s + \sigma_{\psi\psi}^s = \frac{1}{s_{11}^s + s_{12}^s}\left[\Delta u + \frac{Q_{12}s_{11}^s - Q_{11}s_{12}^s}{s_{11}^s - s_{12}^s} \times \times \int_{R_m<\rho<R_i} \frac{2\rho\, d\rho}{R_m^2 - R_i^2} P_3^2(l/2,\rho)\right], \quad \text{(A.9d)}$$

$$\sigma_{\rho\psi} = 0, \quad \sigma_{\rho z} = 0, \quad \sigma_{z\psi} = 0. \quad \text{(A.9e)}$$

Here the difference $\Delta u = u_t^c - u_t^s = \frac{2\mu}{R_o}(s_{11}^s + 2s_{12}^s) + (\vartheta_i^c - \vartheta_i^s)\Delta T - u_g$ is introduced. Let us recap that superscript "s" is related to the shell material, "c" is related to the core. Hereinafter, we suppose that $s_{ij}^s \approx s_{ij}^c \approx s_{ij}$. Invariants:

$$Sp(\sigma_{ii}^c) = -\frac{1}{s_{11} + s_{12}} \times \times \frac{2R_o\Delta h}{(R_o + R_i)h}(2\Delta u + (Q_{12} + Q_{11})P_3^2), \quad \text{(A.10a)}$$

$$Sp(\sigma_{ii}^s) = \frac{1}{s_{11} + s_{12}}\left(2\Delta u + (Q_{12} + Q_{11}) \times \times \int_{R_m<\rho<R_i} \frac{2\rho\, d\rho}{R_m^2 - R_i^2} P_3^2(l/2,\rho)\right), \quad \text{(A.10b)}$$

$$\sigma_{ii}^{s\,2} \approx \frac{1}{(s_{11} + s_{12})^2}\left[\Delta u^2 + 2\Delta u(Q_{11} + Q_{12}) \times \times \int_{R_m<\rho<R_i} \frac{2\rho\, d\rho}{R_m^2 - R_i^2} P_3^2(l/2,\rho) + \right. \\ \left. + \frac{(Q_{11}^2 + Q_{11}^2)(s_{11}^2 + s_{12}^2) - 4Q_{11}Q_{12}s_{11}s_{12}}{(s_{11} - s_{12})^2} \times \times \left(\int_{R_m<\rho<R_i} \frac{2\rho\, d\rho}{R_m^2 - R_i^2} P_3^2(l/2,\rho)\right)^2\right]. \quad \text{(A.10c)}$$

Using (A.10) and the condition $\Delta h << h$, the polarization dependent part of the core free energy expansion (A.1) acquires the form:

$$G_V \approx \int_{-l/2}^{l/2} dz \int_0^{2\pi} d\psi \int_{R_i}^{R_o-\Delta h} \rho d\rho \times \times \left(\left(a_1 + (Q_{11} + Q_{12})\frac{\Delta u}{s_{11} + s_{12}} \frac{2R_o\Delta h}{(R_o + R_i)h}\right)P_3^2 + a_{111}P_3^6 + \right. \\ \left. + \left(a_{11} + \frac{2R_o\Delta h}{(R_o + R_i)h} \frac{(Q_{11}^2 + Q_{12}^2)s_{11} - 2Q_{11}Q_{12}s_{12}}{2(s_{11}^2 - s_{12}^2)}\right)P_3^4\right). \quad \text{(A.11)}$$

In Eq. (A.11) we neglected the terms proportional $(\Delta h / h)^2$.

Table 2.

Parameters of single crystals	PZT 50/50
T_C (K)	666
α_T (10^5 m F^{-1} K^{-1})	2.66
β (10^8 m^5 F^{-1} C^{-2})	1.898
γ (10^8 m^9 F^{-1} C^{-4})	8.016
Q_{11} (m^4 C^{-2})	0.097
Q_{12} (m^4 C^{-2})	–0.046
s_{11} (10^{-12} m^2 N^{-1})	10.5
s_{12} (10^{-12} m^2 N^{-1})	–3.7
ε_{11}; ε_{33}	1700; 730

PZT bulk values d_{31} = –93.5 pm/V, d_{15} = 494 pm/V, d_{33} = 220 pm/V, ε_{11} = 1180, ε_{33} = 730. BTO bulk values d_{13} = –34.5 pm/V, d_{33} = 86 pm/V, d_{15} = 392 pm/V, ε_{11} = 2920, ε_{33} = 168.

References

1. D. Yadlovker and S. Berger, Uniform orientation and size of ferroelectric domains // *Phys. Rev. B* **71**, 184112 (2005).
2. G. Geneste, E. Bousquest, J. Junquera, and P. Chosez, Finite-size effects in $BaTiO_3$ nanowires // *Appl. Phys. Lett.* **88**, 112906 (2006).
3. Y. Luo, I. Szafraniak, N.D. Zakharov, V. Nagarajan, M. Steinhart, R.B. Wehrspohn, J.H. Wendroff, R. Ramesh, M. Alexe, Nanoshell tubes of ferroelectric lead zirconate titanate and barium titanate // *Appl. Phys. Lett.* **83**, p. 440 (2003).
4. D. Morrison, L. Ramsay, and J.F. Scott, High aspect ratio piezoelectric strontium-bismuth-tantalate nanotubes // *J. Phys.: Condens. Matter* **15**, p. L527 (2003).
5. F.D. Morrison Y. Luo, I. Szafraniak, *et al*., Ferroelectric nanotubes // *Rev. Adv. Mater. Sci.* **4**, p. 114 (2003).
6. M.E. Lines and A.M. Glass, *Principles and Applications of Ferroelectrics and Related Phenomena.* Clarendon Press, Oxford, 1977.
7. L.D. Landau and E.M. Lifshits, *Electrodynamics of Continuous Media*. Butterworth Heinemann, Oxford, 1980.
8. D.R. Tilley, *Finite-size effects on phase transitions in ferroelectrics*, In: *Ferroelectric Thin Films*, ed. C. Paz de Araujo, J.F. Scott, and G.W. Teylor. Gordon and Breach, Amsterdam, 1996.
9. C.L. Wang and S.R.P. Smith, Landau theory of the size-driven phase transition in ferroelectrics // *J. Phys.: Condens. Matter* **7**, p. 7163 (1995).
10. I. Rychetsky and O. Hudak, The ferroelectric phase transition in small spherical particles // *J. Phys.: Condens. Matter* **9**, p. 4955 (1997).
11. D.D. Fong, G.B. Stephenson, S.K. Streiffer, J.A. Eastman, O. Auciello, P.H. Fuoss, and C. Thompson, Ferroelectricity in ultrathin perovskite films // *Science* **304**, p. 1650 (2004).
12. S.K. Mishra and D. Pandey, Effect of particle size on the ferroelectric behaviour of tetragonal and rhombohedral $Pb(Zr_xTi_{1-x})O_3$ ceramics and powders // *J. Phys.: Condens. Matter* **7,** p. 9287 (1995).
13. K. Uchino, E. Sadanaga, and T. Hirose, Dependence of the crystal structure on particle size in barium titanate // *J. Amer. Ceram. Soc.* **72**, p. 1555 (1989).
14. M.D. Glinchuk and A.N. Morozovska, Effect of surface tension and depolarization field on ferroelectric nanomaterials properties // *Phys. status solidi* (*b*) **238**, p. 81 (2003).
15. H. Huang, C.Q. Sun, Zh. Tianshu and P. Hing, Grain-size effect on ferroelectric $Pb(Zr_{1-x}Ti_x)O_3$ solid solutions induced by surface bond contraction // *Phys. Rev. B* **63**, 184112 (2001).
16. E.D. Mishina, K.A. Vorotilov, V.A. Vasil'ev, A.S. Sigov, N. Ohta, and S. Nakabayashi, Porous silicon-based ferroelectric nanostructures // *Zhurnal. Experim. Teor. Fiziki* **95** (3), p. 502-504 (2002) (in Russian).
17. R. Poyato and B.D. Huey and N.P. Padture, Local piezoelectric and ferroelectric responses in nanotube-patterned thin films of BaTiO3 synthesized hydrothermally at 200 °C // *J. Mater. Res.* **21**, 547 (2006).
18. A.N. Morozovska, E.A. Eliseev, and M.D. Glinchuk, Ferroelectricity enhancement in confined nanorods: Direct variational method // *Phys. Rev. B* **73**, 214106 (2006).
19. A.N. Morozovska, E.A. Eliseev, and M.D. Glinchuk, Size effects and depolarization field influence on the phase diagrams of cylindrical ferroelectric nanoparticles // *Physica B* **387**, p. 358 (2007).
20. A.N. Morozovska, M.D. Glinchuk, and E.A. Eliseev, Ferroelectricity enhancement in ferroelectric nanotubes // *Phase Transitions* **80**, No. 1-2, p. 71-77 (2007).
21. J. Freund, J. Halbritter, and J.K.H. Horber, How dry are dried samples? Water adsorption measured by STM // *Microsc. Res. Tech.* **44**, p. 327-338 (1999).
22. R. Kretschmer and K. Binder, Surface effects on phase transition in ferroelectrics and dipolar magnets // *Phys. Rev. B* **20**, p. 1065 (1976).
23. J.C. Niepce, Permittivity of fine grained $BaTiO_3$ // *Electroceramics* **4**, No. 5-7, p. 29 (1994).
24. P. Perriat, J.C. Niepce, G. Gaboche, Thermodynamic consideration of the grain size dependence of materials properties // *J. Thermal Analysis* **41**, p. 635-649 (1994).
25. M.D. Glinchuk, A.N. Morozovska, Radiospectroscopy and dielectric properties of nanomaterials // *Fizika tverdogo tela* **45** (8), p. 1510-1518 (2003) (in Russian).
26. V.A. Shchukin and D. Bimberg, Spontaneous ordering of nanostructures on crystal surfaces // *Reviews of Modern Physics* **71** (4), p. 1125-1171 (1999).
27. S.V. Kalinin, E.A. Eliseev, and A.N. Morozovska, Materials contrast in piezoresponse force microscopy // *Appl. Phys. Lett.* **88**, p. 232904-1-3 (2006).
28. A.N. Morozovska, S.V. Svechnikov, The influence of size effects on thin films local piezoelectric response // *Semiconductor Physics, Quantum Electronics & Optoelectronics* **10** (4), p. 36-41 (2007).
29. L.D. Landau and E.M. Lifshitz, *Theory of Elasticity. Theoretical Physics*, Vol. 7. Butterworth-Heinemann, Oxford, U.K., 1998.
30. N.A. Pertsev, A.G. Zembilgotov, and A.K. Tagantsev, Effect of mechanical boundary conditions on phase diagrams of epitaxial ferroelectric thin films // *Phys. Rev. Lett.* **80** (9), p. 1988-1991 (1998).

31. J.S. Speck, and W. Pompe, Domain configurations due to multiple misfit relaxation mechanisms in epitaxial ferroelectric thin films. I. Theory // *J. Appl. Phys.* **76** (1), p. 466-476 (1994).
32. B.J. Rodriguez, S. Jesse, A.P. Baddorf, and S.V. Kalinin, High resolution electromechanical imaging of ferroelectric materials in a liquid environment by piezoresponse force Microscopy // *Phys. Rev. Lett.* **96** (23), 237602 (2006).
33. A.N. Morozovska, S.V. Svechnikov, E.A. Eliseev, and S.V. Kalinin, Extrinsic size effect in piezoresponse force microscopy of thin films // *Phys. Rev. B* **76** (5), 054123-1-5 (2007).
34. A.N. Morozovska, E.A. Eliseev, G.S. Svechnikov, V. Gopalan, and S.V. Kalinin, Effect of the intrinsic width on the piezoelectric force microscopy of a single ferroelectric domain wall // *J. Appl. Phys.* **103** (12), 124110-1-8 (2008).
35. A.N. Morozovska, E.A. Eliseev, S.L. Bravina, and S.V. Kalinin, Resolution function theory in piezoresponse force microscopy: domain wall profile, spatial resolution, and tip calibration // *Phys. Rev. B* **75** (17), 174109-1-18 (2007).
36. A.N. Morozovska, S.V. Svechnikov, E.A. Eliseev, S. Jesse, B.J. Rodriguez, S.V. Kalinin, Piezoresponse Force Spectroscopy of Ferroelectric-Semiconductor Materials // *J. Appl. Phys*. **102** (11), 114108-1-14 (2007).
37. A.N. Morozovska, S.V. Kalinin, E.A. Eliseev, V. Gopalan, and S.V. Svechnikov, The interaction of an 180-degree ferroelectric domain wall with a biased scanning probe microscopy tip: effective wall geometry and thermodynamics in Ginzburg-Landau-Devonshire theory // *Phys. Rev. B* **78** (12), 125407-1-11 (2008).